Visual Abstract

Crack simulation for the cover of the landfill – A seismic design

Abdoullah Namdar, Mehran Karimpour-Fard*
School of Civil Engineering, Iran University of Science and Technology (IUST), Narmak, Tehran, Iran
ab_namdar@mail.iust.ac.ir, Karimpour_mehran@iust.ac.ir

Omer Mughieda
Department of Civil Engineering Abu Dhabi University, Abu Dhabi, UAE
omer.mughieda@adu.ac.ae

Filippo Berto
Department of Chemical Engineering Materials Environment, Sapienza - Università di Roma, Via Eudossiana, 18 00184 Roma, Italy
filippo.berto@uniroma1.it

Nurmunira Muhammad
Faculty of Civil Engineering Technology, Universiti Malaysia Pahang, Malaysia
aira.munira@gmail.com

ABSTRACT. The stability of the landfill is an environmental issue. The collapse of the landfill causes environmental pollution and influences human life. In the present study, the crack on the cover of the landfill was simulated. Rankine's theory and the Phantom Node Method were used for the simulation length of the crack and the mechanism of the crack propagation in the nonlinear extended finite element method (NXFEM). Artificial Neural Networks (ANNs) based on Levenberg-Marquardt Algorithm and Abalone Rings Data Set mode were used to predict displacement in critical points of the model. The vibration mechanism of the landfill was changed in each model. During applying seismic load on the model, the optimized thickness of the clay cover on the landfill was discussed. The thickness of the landfill cover controls the seismic response of the landfill. The numerical simulation shows differential displacement of the landfill impacts on the crack propagation and the need for the appropriate design of the cover thickness of the landfill.

KEYWORDS. Landfill; Crack, Rankine's theory, Phantom Node Method Displacement, Cover Thickness.

OPEN ACCESS

Citation: Namdar, A., Krimpour-Fard, M., Mughieda, O., Berto, F., Muhammad, N., Crack simulation for the cover of the landfill – A seismic design, Frattura ed Integrità Strutturale, 65 (2023) 112-134.

Received: 22.04.2023
Accepted: 23.05.2023
Online first: 26.05.2023
Published: 01.07.2023

INTRODUCTION

A growing amount of municipal solid waste (MSW) is being produced due to the industrialization of many urban areas [1], resulting in a massive accumulation of MSW and new landfill construction.
Due to changes in the local climate, MSW's physical, chemical, and biological processes can also be affected. As a result of MSW accumulation, high temperatures are generated, which are associated with climate change [2]. During the cover process for landfills with clay, topsoil tends to be more influenced by temperature, and this happens more often in tropical regions, where the soil is exposed to higher temperatures [3]. As temperatures increase in the landfill, cracks form in the clayey cover [2–5], which extend to the body of the landfill [4-5], causing a change in the moisture content of the landfill. Also, during the rainy season, the amount of leachate increases. In the event of seismic loading, landfill cover cracks extend more rapidly, resulting in a reduction in landfill seismic stability.
The landfill's seismic stability is related to local site conditions [6]. Due to the seismic load on the landfill, the damage is divided into major, significant, moderate, minor, slight, or no damage. The crack initiates and occurs in the landfill cover if the damage is moderate. Once the type of damage is recognized, geosynthetics can be utilized to improve landfill seismic stability [7]. Seismic loading causes landfill displacement, and it has been suggested that this phenomenon be quantified through Newmark's one-dimensional analytical sliding-block method [8]. Many researchers have applied the nonlinear finite element method to calculate the nonlinear displacement of the embankment model [9]. Using the appropriate method to simulate a landfill's seismic response accurately is essential.
Further, it must be noted that the material's mechanical properties and the model's geometry properties have an impact on the displacement mechanism, and these properties need to be understood correctly by evaluating the input data accurately [10–12]. It is well known that the calculation of seismic deformation caused by an earthquake is prone to some error levels [13–15]. The impact of seismic loading on the displacement of the landfill has been systematically investigated to identify the seismic stability of the landfill [16–18]. Landfill displacement could be minimized using geomembrane [19–20], lattice drainage geocomposite, and flexible polyester [20]. Aside from these methods, clay soil is also used to cover landfills [21, 22]. The compacted soil liner (CSL) is required to control a hydraulic conductivity of ($\leq 1 \times 10-7$ cm/s); for this purpose, clay with a thickness in the range of 0.6 to 1.5 m is required [24, 25]. Displacement prediction is needed before applying the seismic mitigation method to improve landfill seismic stability. Nonlinear numerical simulations can identify displacement at any point in the modeled landfill. Due to the nonlinearity of the seismic load, numerical simulation results need to be validated using statistical analysis.
The current study used artificial neural networks to predict embankment displacement [11–12, 26]. The prediction is made from the validation and optimization results of the numerical simulation [27–29]. The main objective of the present study is to consider the impact of cracked landfill covers with different thicknesses on the displacement of two critical points in the model. In order to predict displacement at selected points in the model, the Levenberg-Marquardt algorithm was used, which considers Rankine's theory and the phantom node method in crack simulation and propagation.

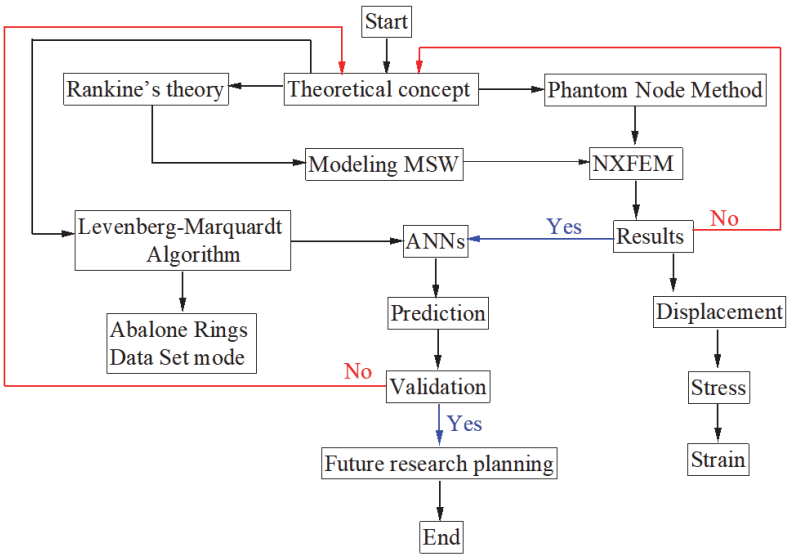

Figure 1: The entire numerical simulation steps.

MODELING

Soil-like materials (SLM) such as MSW are highly deformable under seismic loading. The crack initiation on the landfill cover was simulated and shown in Fig. 1, which illustrates the entire numerical simulation procedure. Numerical modeling was conducted to design the clay landfill cover under seismic loading. Fig. 2 shows the model components, MSW and clay.

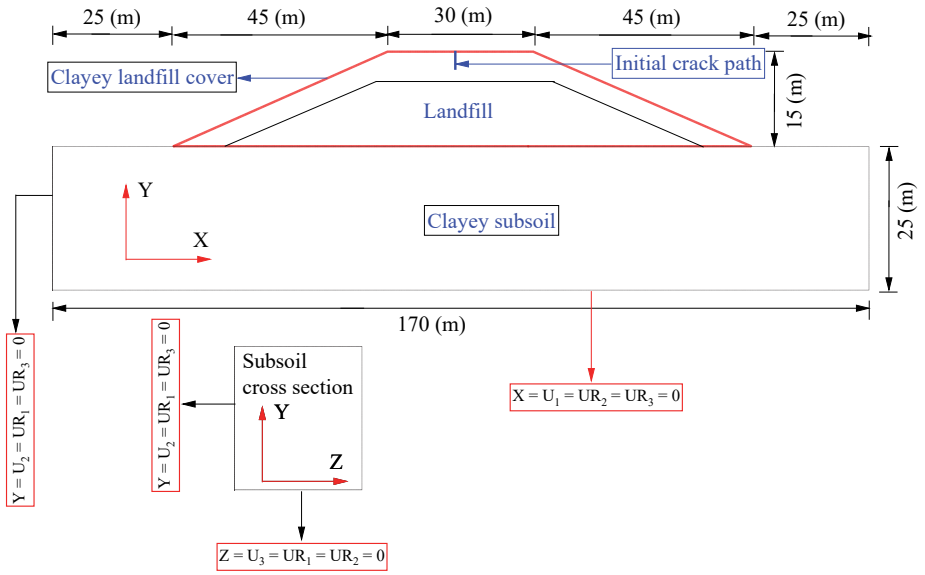

Figure 2: The landfill model with a clay cover, clay subsoil, and boundary conditions used in the numerical simulation.

CRACK SIMULATION

The initial crack in the landfill clay cover is designed based on Rankine's theory (1857) [30]. The crack and solid zones are two significant parts of the model. The ratio of the crack height to the total thickness of the landfill cover for each part changes with respect to the model's mechanical properties. In fact, when the two models have the same geometry but are constructed from two different MSW materials, the crack, and solid zones are changed according to the types of materials used. It is assumed that landfill leachate is confined under undrained conditions.

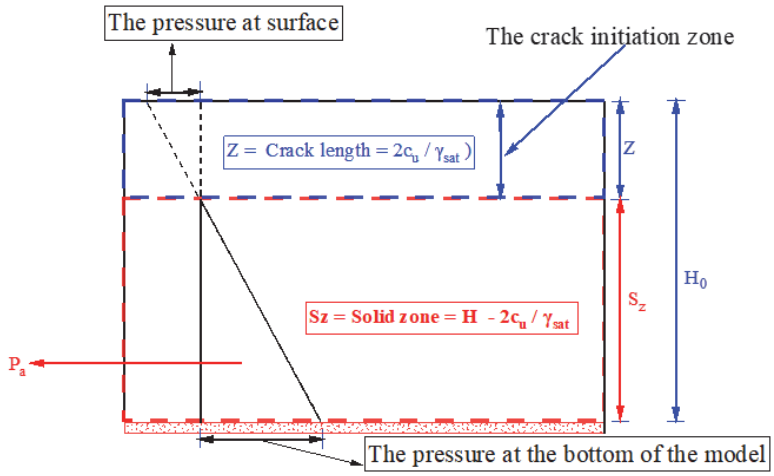

Figure 3: Theoretical crack initiation for the clayey cover of the landfill.

According to Rankine's theory, k_p and k_a are the passive and active earth pressure coefficients and are presented in Eqns. 1 and 2. The pressure and force in the active and passive states have been explained in Eqns. 1-12 [31].

$$k_p = \frac{1+\sin\phi'}{1-\sin\phi'} \tag{1}$$

$$k_a = \frac{1-\sin\phi'}{1+\sin\phi'} \tag{2}$$

From Eqns. 1 and 2, Eqn. 3 can be written.

$$k_p = \frac{1}{k_a} \tag{3}$$

where the Rankine active state in the slip plane is,

$$\theta_a = 45^\circ + \frac{\phi'}{2} \tag{4}$$

where the Rankine passive state in the slip plane is,

$$\theta_p = 45^\circ - \frac{\phi'}{2} \tag{5}$$

The lateral earth pressure for the Rankine active state is,

$$\left(\sigma_x'\right)_a = K_a\sigma_z' = K_a\gamma' z \tag{6}$$

The lateral earth pressure for Rankine passive state is,

$$\left(\sigma_x'\right)_p = K_p\sigma_z' = K_p\gamma' z \tag{7}$$

$$\gamma' = \left(\gamma_{sat} - \gamma_w\right) \tag{8}$$

The lateral earth force in Rankine's active state is,

$$P_a = \int_0^{H_0} K_a\gamma' z = \frac{1}{2}K_a\gamma' H_0^2 \tag{9}$$

The lateral earth force in Rankine's passive state is,

$$P_p = \int_0^{H_0} K_p\gamma' z = \frac{1}{2}K_p\gamma' H_0^2 \tag{10}$$

For the undrained condition in a fully saturated clay, the active and passive pressures are calculated using the parameter c_u, (ϕ_u is equal to zero) and the total unit weight γ_{sat}. When enough deformation occurs the state of plastic equilibrium occurs. Eqns. 11 and 12 have been used to identify the length of the crack, the solid zone, and the crack initiation zone [32].

$$Z = Cracked\ zone = 2c_u / \gamma \quad (11)$$

$$S_z = Solid\ zone = H_0 - Z \quad (12)$$

Based on the theoretical concepts, the crack initiates in association with the mechanical properties of the clay. The crack propagation caused by applying an external load on the model was simulated. Fig. 3 illustrates the crack and solid zone in the landfill cover.

SEISMIC DATA

According to the literature report [33], to achieve acceptable results multidirectional seismic acceleration needs to be applied to the model in the numerical simulation. By applying one direction of seismic acceleration to the model, the underestimated strain, stress, and displacement would be obtained in the numerical simulation. Fig. 4 illustrates the multidirectional acceleration history (m/s²) used in NFEM.

The seismic acceleration at 0°, 90°, and 360° of the Abra Pampa Earthquake, which occurred on 22 Feb 2022, with 6.0 MWW, in coordinates -22.6625 and -66.2673 in a depth of 242.3 km [34], has been used as the input data in the nonlinear numerical simulation. The seismic accelerations applied to models 1 and 2 are equal. The seismic acceleration in each direction has minimum and maximum domains. The combination of these three accelerations needs to be applied to the model. The critical duration of seismic acceleration at 0°, 90°, and 360° is shown in Fig. 4. The shaking over 0.05 (g) in positive and negative directions in all directions is the most unpleasant and needs to be considered in the nonlinear numerical simulation. Tab. 1 shows peak ground acceleration, displacement, and velocity at 0°, 90°, and 360°.

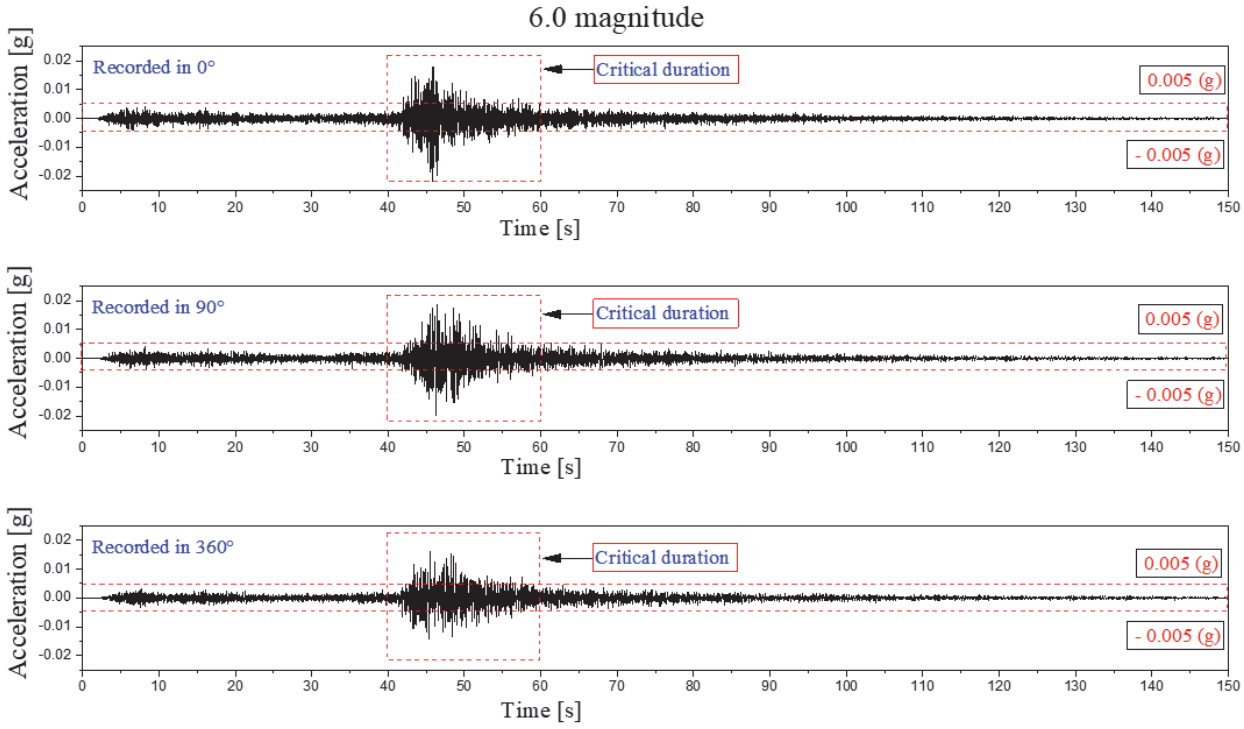

Figure 4: The multidirectional acceleration history (m/s²) used in NFEM [34].

Direction	Peak ground acceleration [g]	Peak ground velocity [cm/sec]	Peak ground displacement [cm]
0°	- 0.0222	0.7732	0.0334
90°	-0.0203	- 0.8904	0.0419
360°	0.0165	0.492	0.0257

Table 1: Earthquake data [34].

MECHANICAL PROPERTIES

MSW mechanical properties are reported in the literature. Tab. 2 illustrates the mechanical properties of MSW used to simulate landfills [35–37]. MSW is a highly deformable material with a high compressibility level. The MSW elasticity modulus has been calculated using Eqn. 13.

$$E = 2G(1+\nu) \tag{13}$$

Material	Friction angle, ϕ (deg)	Cohesion, C (kPa)	Poisson's ratio, ν	Unit weight, γ (kN/m³)	Modulus elasticity, E (MPa)	Shear modulus, G (MPa)
MSW	34	22	0.33	14.93	5.61	2.11

Table 2: Mechanical properties of the MSW [35-37].

The angle of internal friction for clay under undrained conditions is assumed to be equal to zero ($\phi_u = 0$) [38]. The unit weight of undrained clay (γ_c) is 18 (kN/m³). The undrained modulus of elasticity (E_u) is 12.5 MPa. Poisson's ratio ν_c of 0.3 and undrained shear strength equal to 25 kPa have been reported in the literature [39]. The model has three parts, the subsoil, the landfill, and the cover of the landfill. The landfill subsoil and cover were designed using clay. The Landfill has been simulated using MSW.

NONLINEAR EXTENDED FINITE ELEMENT METHOD AND CRACK PROPAGATION

The XFEM provides a situation in that discontinuities act independently, and different types of discontinuities are generating [40]. The crack simulation using XFEM was reported in the literature [41-42]. Eqn. 14 presents the standard form of XFEM [43-44].

$$u^h(x) = \sum_{i\in I} N_i(x)u_i + \sum_{i=\in I^*} N_i^*(x)\,.\tilde{N}\mp(x).a_i \tag{14}$$

The phantom node method for modeling fracture is introduced. This technique involves intersecting elements by a crack, erasing the crack, and replacing it with two new elements without modifying the original location of the element. This process does not alter the physical characteristics of the material [45], and later it was upgraded by using a more advanced technique [46]. In the present work, using ABAQUS, the phantom node method has been adopted to simulate crack propagation in the landfill cover.

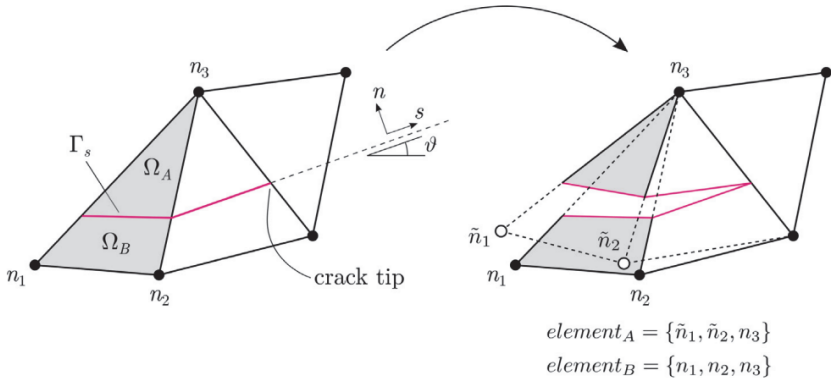

Figure 5: The phantom node method in mesh generation [47].

Fig. 5 explains nodes, elements, and meshes generation by the phantom node method [47], in this process the elements have independent displacement without sharing nodes [48]. Considering Fig. 5, according to the phantom node method, to explain the discontinuous displacement for overlapping elements can be written as [47],

$$U(X)=\begin{cases}N(X)U_A, x\in\Omega_A\\ N(X)U_B.\ \ x\in\Omega_B\end{cases} \tag{15}$$

$$U(X)=N(X)(U_A-U_B),\ X\in\Gamma_s \tag{16}$$

where Γ_s presents the crack path, $\Omega_{A,}$ and Ω_B refer to the shaded area the portion of a new element A and B respectively. The N is the standard for finite element method shape functions and U_A and U_B are the displacements in nodes A and B. Fig. 2 illustrates the boundary condition adopted and applied in the numerical simulation. Two models of the landfill with the cracked cover are simulated. The smallest mesh size is selected for landfill cover. The mesh sizes of 2000 (mm), 4000 (mm), and 6000 (mm) have been selected for landfill cover, landfill, and subsoil of the model respectively. The geometry of the mesh is shown in Fig. 6. The MSW has been covered with clay. In model 1 the cover of the landfill is 3 (m), and in the second model, the cover of the landfill is increased to 6 (m). The selected nodes in numerical simulation for models 1 and 2 are shown in Fig. 6. In these two critical points the displacement, stress, and strain will be analyzed in the next part of the present study.

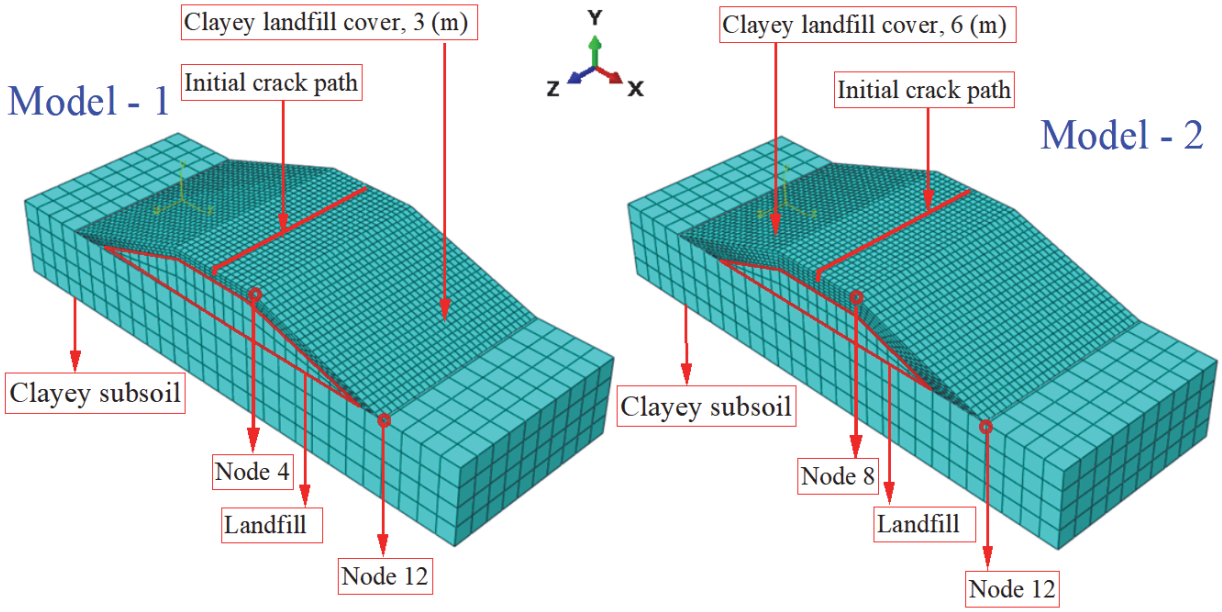

Figure 6: Mesh design in the numerical simulation.

ARTIFICIAL NEURAL NETWORKS

Artificial neural networks (ANNs) are frequently employed for geotechnical engineering problem prediction, assessment, and solution [12, 26]. ANNs are employed in data prediction, categorization, association, and filtering [49]. The Levenberg-Marquardt algorithm was used in this study to perform ANNs for classification and prediction. The four key criteria for predicting displacement are seismic acceleration, stress, strain, and fracture length. The thickness of the landfill cover was varied in the numerical simulation, but the seismic acceleration and model geometries were fixed for models 1 and 2. In MATLAB, Artificial Neural Networks (ANNs) were utilized to forecast displacement in the Y direction of the chosen object. The ANNs in different layers were done, and the numerical simulation results were checked, validated, and predicted based on the training to reach the best outcomes for displacement occurrence.
Eqns. 17-18 introduce the basic concept of the Levenberg-Marquardt Algorithm [50]. If α,β,γ are unknown parameters at points $(x_i,\ y_i,\ z_i,\ldots)$

$$f_i(\alpha,\beta,\gamma,\ldots)=H(x_i,\ y_i,\ z_i,\ldots;\alpha,\beta,\gamma,\ldots)-h(x_i,\ y_i,\ z_i,\ldots) \tag{17}$$

Eqn. 17, can be minimized to

$$S(\alpha,\beta,\gamma,\ldots)=\sum_{1}^{n} f_i^2 \tag{18}$$

The Hessian matrix is presented in Eqns. 19-20. If *f*: $R^n \rightarrow R$ presents a function for input $X \in R^n$ and output $f(X) \in R$. If partial derivation f is available, subsequently the Hessian matrix H is a square matrix [51].

$$H_f=\begin{bmatrix} \frac{\partial^2 f}{\partial x_1^2} & \frac{\partial^2 f}{\partial x_1 \partial x_2} & \cdots & \frac{\partial^2 f}{\partial x_1 \partial x_n} \\ \frac{\partial^2 f}{\partial x_2 \partial x_1} & \frac{\partial^2 f}{\partial x_2^2} & \cdots & \frac{\partial^2 f}{\partial x_2 \partial x_n} \\ \vdots & \vdots & \ddots & \vdots \\ \frac{\partial^2 f}{\partial x_n \partial x_1} & \frac{\partial^2 f}{\partial x_n \partial x_2} & \cdots & \frac{\partial^2 f}{\partial x_n^2} \end{bmatrix} \tag{19}$$

$$\left(H_f\right)_{ij}=\frac{\partial^2 f}{\partial x_i \partial x_j} \tag{20}$$

where J presents the Jacobian matrix the Hessian matrix H is

$$H=J^T J \tag{21}$$

If "e" is selected as a vector of network errors, the gradient will be calculated from Eqn. 22,

$$g_k=J^T e \tag{22}$$

The Updated weights in the Levenberg-Marquardt algorithm can be as

$$W_{k+1}=W_k-\left[J^T J+\mu I\right]^{-1} J^T e \tag{23}$$

To approach second-order training without employing the Hessian matrix, the Levenberg-Marquardt technique was presented [52]. In light of the statistical idea offered in the literature [53], Eqns. 24-25 are proposed. d is the acquired nonlinear displacement in the numerical simulation, d_p is the projected displacement using ANNs, and $\bar{D}_o$ is the mean value of obtained nonlinear displacement in these two equations. The accuracy of displacement prediction was assessed using Eqns. 24- 25.

$$MSE=\frac{1}{n}\sum_{i=1}^{n}\left(d-d_p\right)^2 \tag{24}$$

$$R^2=1-\frac{\sum_{i=1}^{n}\Sigma\left(d-d_p\right)^2}{\sum_{i=1}^{n}\Sigma\left(d-\bar{D}_o\right)^2} \tag{25}$$

RESULTS AND DISCUSSIONS

A nonlinear numerical simulation was performed to predict the nonlinear displacement at two critical points in the landfill. The results of the nonlinear numerical simulation showed that the speed and shape of the deformation in each model have distinct behaviors. MSW is a highly deformable material. Because of this characteristic, when MSW is subjected to seismic acceleration, it has a different seismic response compared to clay. Fig. 7 illustrates the nonlinear shear stress-strain for a particular node. These points have been selected for monitoring displacement in the subsoil, the clayey cover of the landfill, and the main body of the landfill. Fig. 8 illustrates the multidirectional nonlinear acceleration-displacement in the Y direction for a selected node in models 1 and 2. Figs. 7 and 8 reveal the MSW-clay interface's impact on the model's seismic response. In addition, landfill covers of different thicknesses exhibit higher seismic resistance. In addition, models 1 and 2 have different deformability. The unique deformation pattern for each model was observed. According to the nonlinear shear stress-strain curve, model 2 collapses with lower deformation. Increasing the clay landfill cover by more than 3 meters reduces seismic stability. The displacement at the crest and toe of the landfill is dissimilar. The clay landfill cover acts as a surcharge on the landfill and increases its displacement.

The seismic frequency causes fill excitation to impact landfill stability considerably [16]. The Abra-Pampa earthquake was simulated and applied to the landfill in the present work. This earthquake has a high frequency. The high frequency of the earthquake accelerates the model collapse before a high displacement level occurs.

Due to the seismic load applied to the landfill, a crack develops on the landfill cover during the moderate damage stage [7]. Figs. 7 and 8 show that the landfill is subject to significant damage within a short period of time. In this mode of landfill damage, crack propagation does not occur in the landfill. The numerical simulations presented in Figs. 7–9 agree with the literature report. The landfill damage occurred based on the model's internal load interaction, the MSW's texture, the surcharge's magnitude, and the landfill design. In addition, the materials' surface interaction controls the seismic load transfer and dissipation patterns.

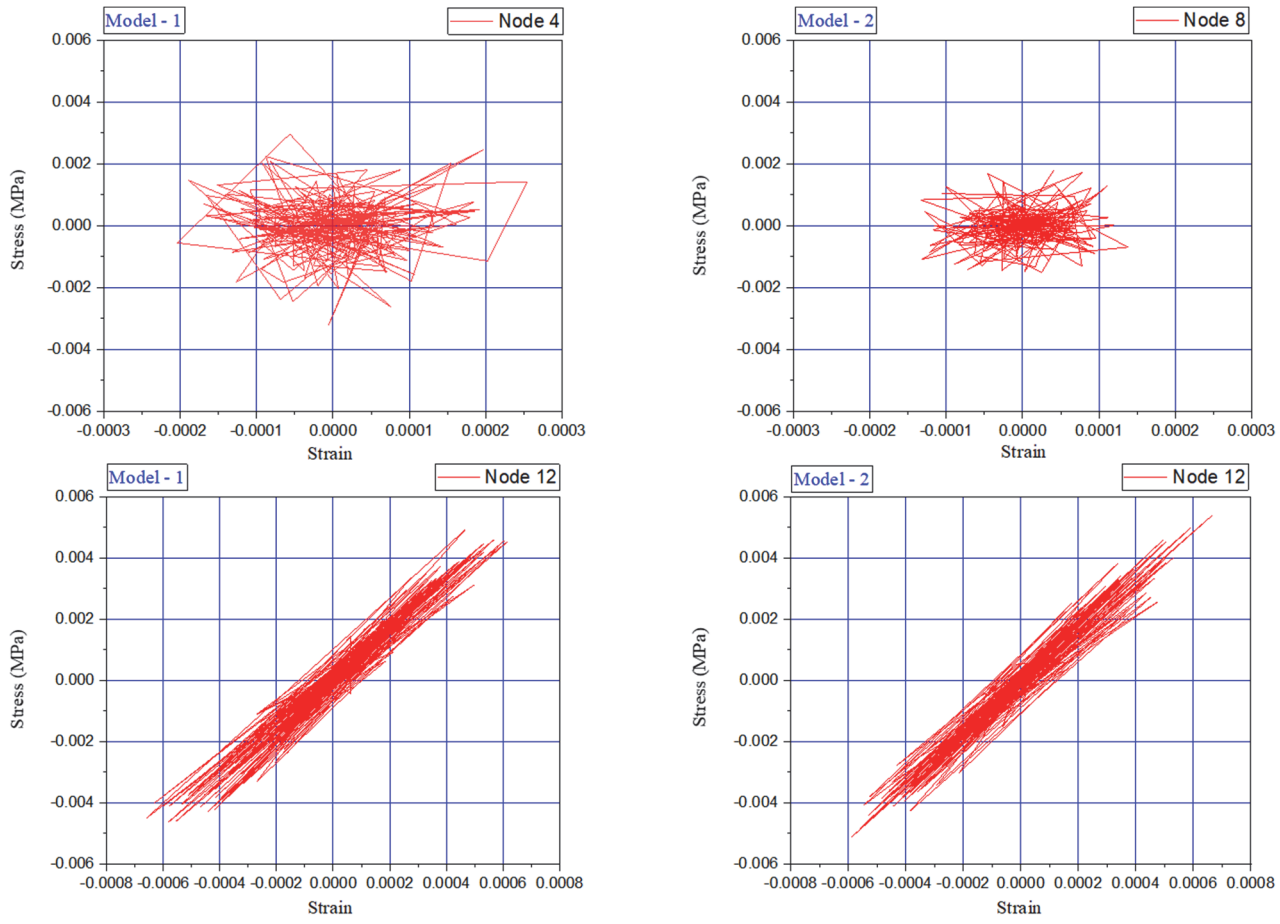

Figure 7: The nonlinear shear stress (MPa) -strain for the selected nodes in models 1 and 2.

By comparing the stress-strain curve, it was possible to determine the reduction of stiffness in model 2. The shear and compressive strain in model 1 at node 4 are larger than in model 2 at the same point. In the loading and reloading stages of models 1 and 2, at embankment and subsoil, stress-strain characteristics follow two different patterns. In both models, the stress-strain rate is higher in the subsoil than in the embankment. The nature of MSW-clay landfill cover interaction causes the development of distinct seismic responses and seismic differential displacement for each model.

In addition, the numerical simulation results revealed that the model's vibration mechanism is associated with the mechanical properties and material design of landfill construction. Due to the characteristics of MSW, two surfaces of cracks interact with each other, which affects displacement and deformation in the landfill.

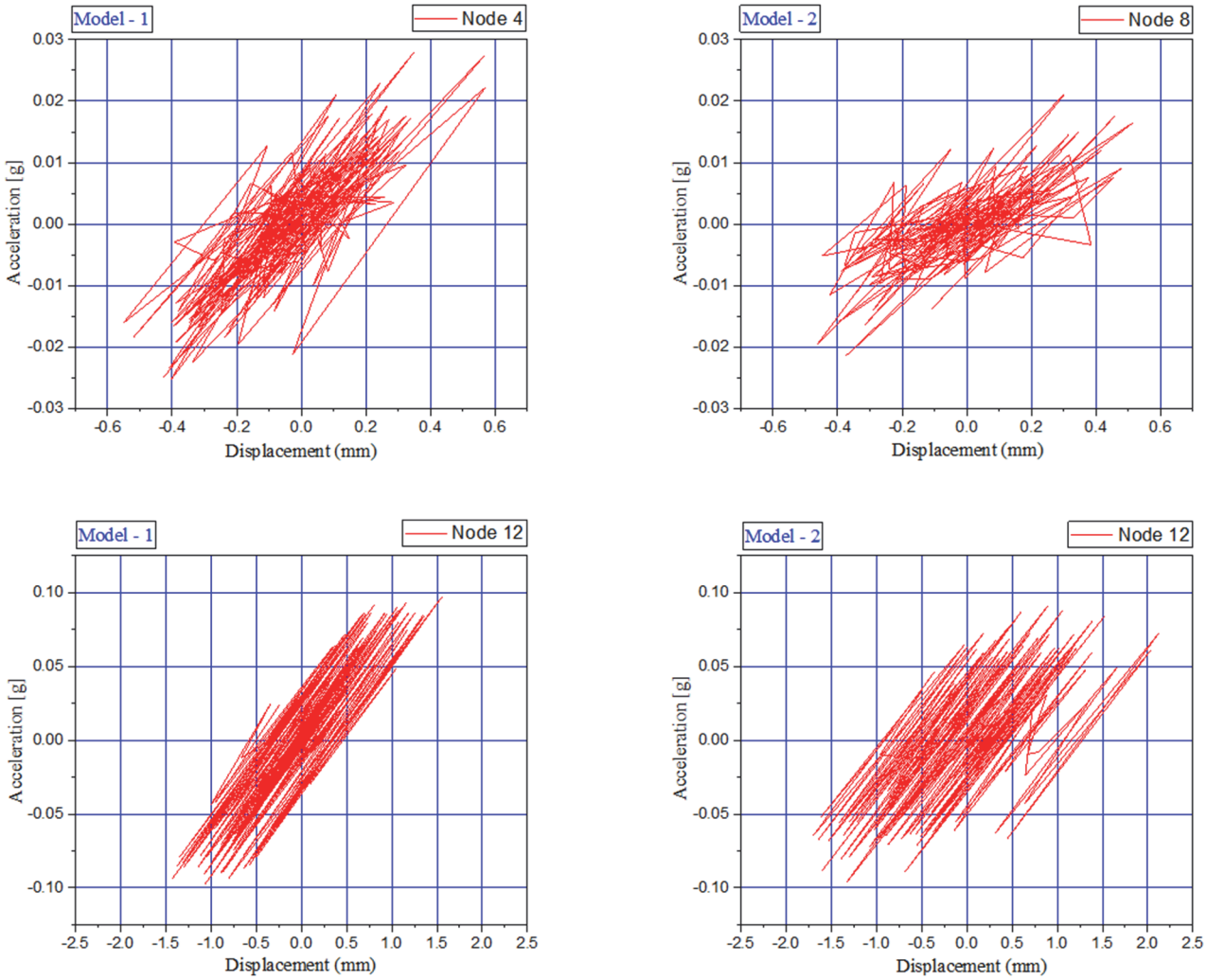

Figure 8: The multidirectional nonlinear acceleration (g) – displacement (mm) in Y direction for the selected node.

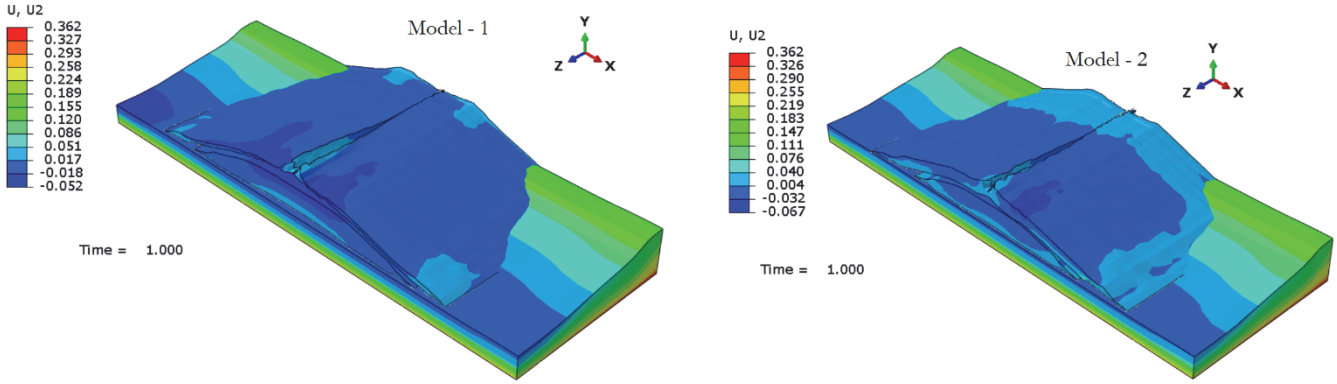

Figure 9: The displacement (mm) after 1 second of applied acceleration (g).

Fig. 9 illustrates the displacement in the whole model after 1 second of applying seismic acceleration (g) to the model. The crack shows different morphology at each stage of the numerical simulation. The nature of the seismic acceleration (g) determines the failure mechanism in both models. In addition, the landfill clay cover thickness controls the crack propagation mechanism. With attention to the difference between lower and higher displacement levels in models 1 and 2, it seems that model 1 has a higher collapsing speed. Fig. 9 shows that the model's failure pattern occurs based on the model's lateral sliding. These similarities in the type of failure in models 1 and 2 occur due to the nature of the seismic acceleration.
The compacted soil liner (CSL) needs to maintain a hydraulic conductivity of ($\leq 1 \times 10{-}7$ cm/s). For this purpose, clay with a thickness in the range of 0.6–1.5 m is required [24–25], but from the seismic design perspective, the appropriate clay thickness needs to be recommended.
Based on this analysis, it can be concluded that the landfill cover thickness needs to be designed to restrict landfill collapse and control leachate as well.

No	Important Vertical Peak Acceleration (g)	Vertical Peak Stress (MPa)	Vertical Peak Strain	Initial crack length (mm)	Vertical Displacement (mm)
1	-0.01317	0.0013	0	2778	0.26664
2	0.01669	-0.0017	-6.57439E-6	2778	0.56451
3	0.01484	-0.00195	-3.985E-6	2778	-0.33746
4	-0.01374	-0.00157	1.58766E-6	2778	-0.32985
5	-0.02729	0.00205	-4.85409E-6	2778	0.30903
6	0.02255	4.3911E-4	-1.27384E-6	2778	-0.35656
7	0.01522	-0.00239	-8.50539E-6	2778	-0.40129
8	-0.01426	-0.00158	3.63012E-6	2778	0.26985
9	0.01475	-0.00168	-4.72572E-6	2778	-0.34188
10	0.016	0.00166	-3.00413E-6	2778	-0.40806
11	-0.01697	0.00147	-7.22713E-6	2778	0.33844
12	-0.01728	-0.00145	-4.9782E-6	2778	-0.52061
13	0.02336	6.57155E-4	2.68205E-6	2778	-0.37203
14	-0.01757	0.00143	2.82432E-6	2778	-0.39019
15	0.01848	-0.00205	-3.12113E-6	2778	0.30296
16	-0.02286	0.0018	-1.99101E-5	2778	-0.34633
17	0.01837	0.00115	-1.35034E-5	2778	0.28762
18	0.01679	0.00142	2.23796E-6	2778	0.32446
19	0.01536	-8.78402E-4	-4.34029E-6	2778	-0.39414
20	-0.01761	8.09171E-4	-9.24661E-6	2778	-0.38885
21	0.01656	-0.00324	4.23915E-6	2778	0.30545
22	0.01925	0.00297	-3.49117E-6	2778	0.32431
23	-0.01507	0.00208	-2.76953E-5	2778	0.56847
24	-0.02218	-4.41188E-4	2.85844E-5	2778	0.25819
25	0.0212	-6.62765E-4	-1.92921E-6	2778	0.26605
26	-0.01928	-0.00184	-2.7582E-5	2778	-0.34673
27	0.01607	-0.00183	-1.40253E-5	2778	-0.40151
28	-0.02097	0.00202	2.64986E-5	2778	-0.39267
29	0.02514	0.00187	-1.5879E-5	2778	0.34885
30	-0.02796	-8.60109E-4	3.01826E-5	2778	-0.42581
31	0.0249	-2.60599E-4	-2.90391E-5	2778	-0.32551
32	0.01613	-0.00144	1.00611E-5	2778	-0.55136

Table 3: Data used in ANNs for model 1 at node 4.

Tabs. 3, 5, 7, and 9 present the peak values of acceleration (g), stress (MPa), strain, and initial length of the crack (mm) obtained from numerical simulation and theoretical concepts. ANNs based on Levenberg-Marquardt algorithms have been used to predict and validate displacement in the Y direction at the critical point. Due to the huge number of outputs produced in the nonlinear numerical simulation, the peak value of the data has been selected and presented.
The Levenberg-Marquardt algorithm in the Abalone Rings Data Set mode was used to validate and predict displacement accuracy in the ANNs process. The test data and results are validated based on the number of training observations in the numerical simulation. In the ANNs, three layers have been created, and mean squared error (MSE) and R have been obtained. Displacement prediction accuracy has been assessed using Eqns. 24 and 25.
Figs. 10, 12, 14, and 16 show the regression analysis for ANNs outcome. Tabs. 4, 6, 8, and 10 present R^2 and MSE values Model 1 and 2 prediction accuracy are associated with R^2 and MSE. According to statistical analysis, the prediction results are acceptable. Figs. 11, 13, 15, and 17 show the accuracy of the predicted displacement quality.

-	Training	Validation	Test	Number of layers in ANNs
R^2	076992	0.76983	0.7849	3
MSE	4.2268	4.1089	4.4893	3

Table 4: R^2 and MSE results of ANNs for model 1 at node 4.

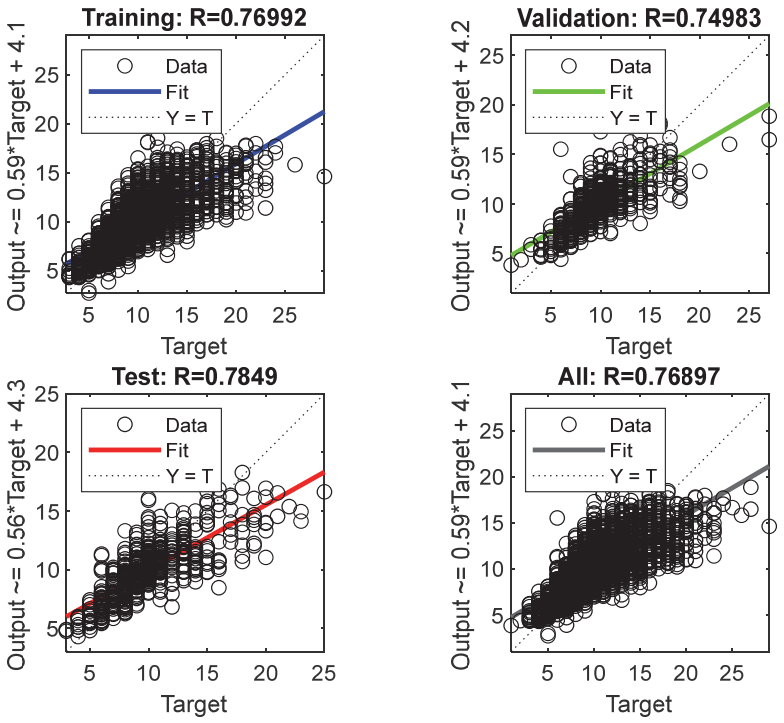

Figure 10: Regression analysis in Y direction of displacement prediction for model 1 at node 4.

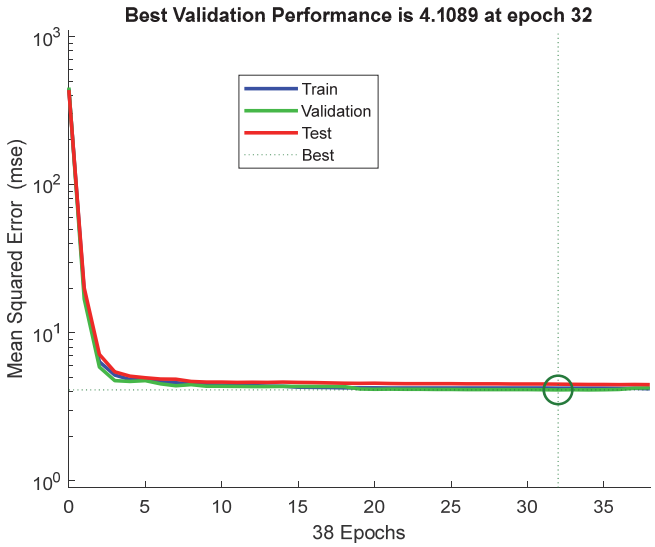

Figure 11: Prediction of displacement in Y direction for model 1 at node 4.

No	Important Vertical Peak Acceleration (g)	Vertical Peak Stress (MPa)	Vertical Peak Strain	Initial crack length (mm)	Vertical Displacement (mm)
1	6.50455E-4	7.92998E-5	-2.69808E-4	2778	0.73177
2	-0.00114	-8.40098E-5	-4.01878E-4	2778	0.70107
3	0.00895	-1.85242E-4	3.51639E-4	2778	0.69455
4	-0.0102	2.81983E-4	-5.36135E-4	2778	0.81327
5	0.02278	-5.08319E-4	4.98431E-4	2778	1.3219
6	-0.02165	3.04166E-4	-4.38268E-4	2778	1.34771
7	-0.02481	-8.2488E-4	5.30683E-4	2778	1.35579
8	0.02566	0.00103	-5.29435E-4	2778	0.99117
9	-0.03778	-0.00121	3.71622E-4	2778	0.94504
10	0.03811	0.00146	-5.83039E-4	2778	1.06602
11	0.0669	-0.0022	6.05269E-4	2778	0.76792
12	-0.0665	0.00204	-4.51155E-4	2778	0.66681
13	-0.08605	0.00298	4.98234E-4	2778	0.73003
14	0.08561	-0.00308	-3.44556E-4	2778	0.66487
15	-0.08479	-0.00367	4.23566E-4	2778	0.68248
16	0.08437	0.0042	-5.32241E-4	2778	1.0571
17	0.09081	-0.00429	6.147E-4	2778	1.1631
18	-0.08763	0.00419	-2.75271E-4	2778	1.07451
19	0.08611	-0.00464	5.82747E-4	2778	0.85982
20	-0.08454	0.00457	-6.60034E-4	2778	0.71614
21	0.09715	-0.00405	5.67388E-4	2778	0.80439
22	-0.09355	0.00453	-5.97126E-4	2778	-0.76087
23	0.09343	-0.00451	5.29893E-4	2778	-0.85938
24	-0.09165	0.00494	-5.78005E-4	2778	-1.14395
25	0.08607	0.00446	-5.11607E-4	2778	-1.23868
26	-0.08637	-0.0041	4.74269E-4	2778	-0.99735
27	-0.08832	0.00403	-5.55682E-4	2778	-0.66179
28	0.08978	-0.00461	-6.29915E-4	2778	-0.88863
29	-0.09711	0.00433	5.37781E-4	2778	0.81259
30	0.09345	-0.00411	-5.07329E-4	2778	1.16592
31	6.50455E-4	-0.00415	4.85554E-4	2778	1.55336
32	-0.00114	0.00398	-5.35886E-4	2778	1.18583

Table 5: Data used in ANNs for model 1 at node 12.

-	Training	Validation	Test	Number of layers in ANNs
R^2	0.74499	0.72808	0.73441	3
MSE	4.6616	5.384	4.1858	3

Table 6: R^2 and MSE results ANNs for model 1 at node 12.

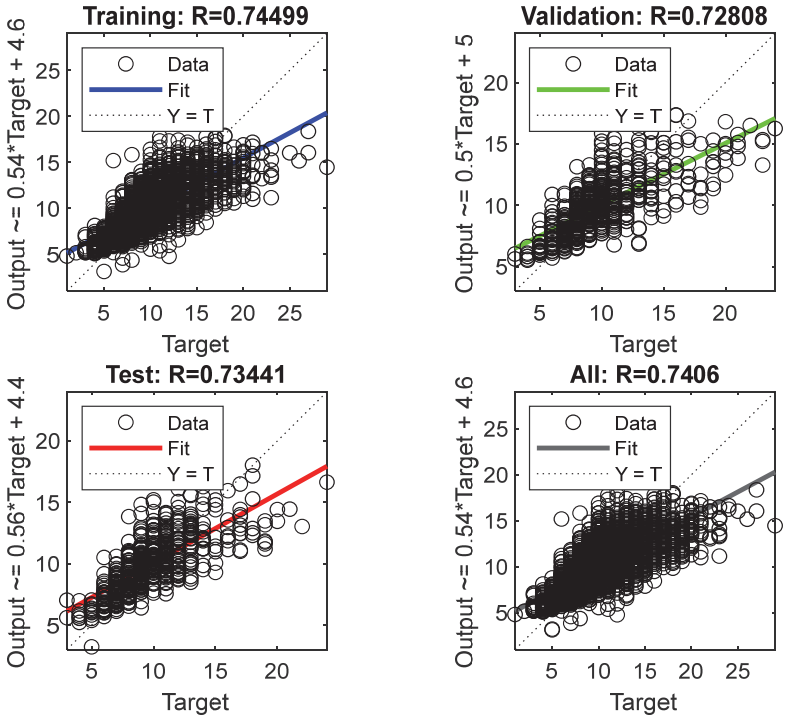

Figure 12: Regression analysis in Y direction of displacement prediction for model 1 at node 12.

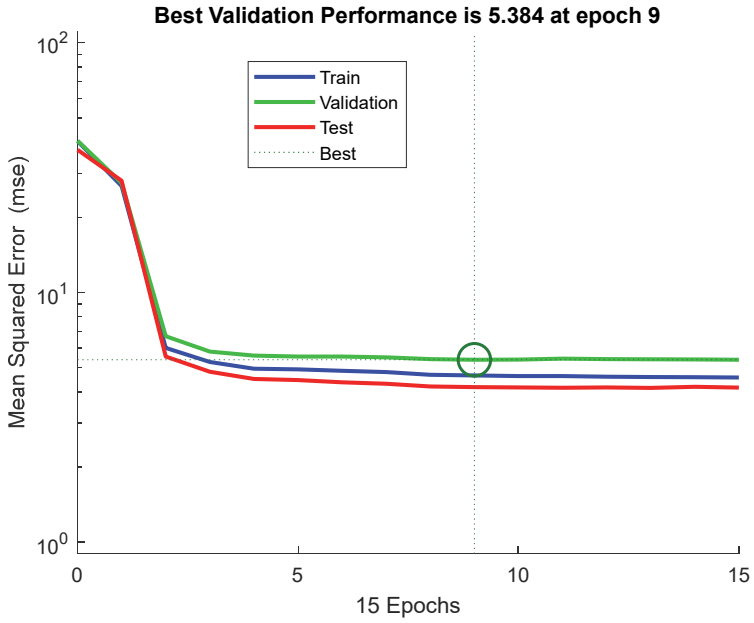

Figure 13: Prediction of displacement in Y direction for model 1 at node 12.

No	Important Vertical Peak Acceleration (g)	Vertical Peak Stress (MPa)	Vertical Peak Strain	Initial crack length (mm)	Vertical Displacement (mm)
1	0.00971	2.47041E-4	-7.65975E-5	2778	-0.29082
2	-0.00975	0.00103	-8.99527E-5	2778	-0.31459
3	0.01633	-0.00125	-1.34125E-4	2778	0.32941
4	0.0084	9.33859E-4	-8.16568E-5	2778	-0.28061
5	0.00994	-8.29053E-4	7.25802E-5	2778	0.45407
6	-0.0091	-0.00101	-8.99114E-5	2778	-0.30253
7	0.00852	-1.1407E-4	1.1234E-4	2778	0.47963
8	-0.00948	-0.00109	-1.02844E-4	2778	0.2593
9	-0.00944	0.00117	1.19955E-4	2778	0.27489
10	0.01398	9.86499E-4	9.62973E-5	2778	-0.38786
11	-0.0123	-8.92837E-4	8.3464E-5	2778	0.25863
12	0.00883	0.0011	9.44113E-5	2778	-0.38438
13	-0.01279	-0.00112	-1.16197E-4	2778	-0.2903
14	0.00864	0.00173	7.87148E-5	2778	-0.29552
15	-0.01205	-0.00152	-1.28119E-4	2778	0.41783
16	0.02132	0.00121	8.95447E-5	2778	0.37678
17	-0.01493	-0.00109	-1.32094E-4	2778	0.38465
18	0.01589	4.41696E-4	8.43624E-5	2778	-0.37205
19	-0.00939	0.00144	-1.21311E-4	2778	0.34543
20	0.01944	0.00144	1.8665E-5	2778	-0.39702
21	-0.02093	-2.79313E-4	9.00824E-5	2778	-0.4609
22	-0.00972	-6.36387E-4	1.0187E-4	2778	0.29921
23	0.0115	0.00107	-2.72714E-5	2778	-0.34462
24	-0.01642	2.5362E-4	8.46645E-5	2778	-0.44756
25	0.00904	-6.92872E-4	1.38161E-4	2778	-0.42403
26	-0.0101	-8.69604E-4	-2.31076E-5	2778	0.51274
27	0.00861	-0.00132	7.77794E-5	2778	0.3122
28	0.01371	0.0018	-1.00841E-4	2778	0.34447
29	-0.01745	8.44321E-4	7.84988E-5	2778	0.45651
30	0.00829	8.44321E-4	-1.17335E-4	2778	0.31465
31	-0.01455	9.8809E-4	-8.36407E-5	2778	-0.33765
32	0.01097	0.00104	8.99673E-5	2778	-0.37807

Table 7: Data used in ANNs for model 2 at node 8.

-	Training	Validation	Test	Number of layers in ANNs
R^2	0.77459	0.79535	0.72027	3
MSE	4.1458	7.0726	4.7931	3

Table 8: R^2 and MSE results ANNs for model 2 at node 8.

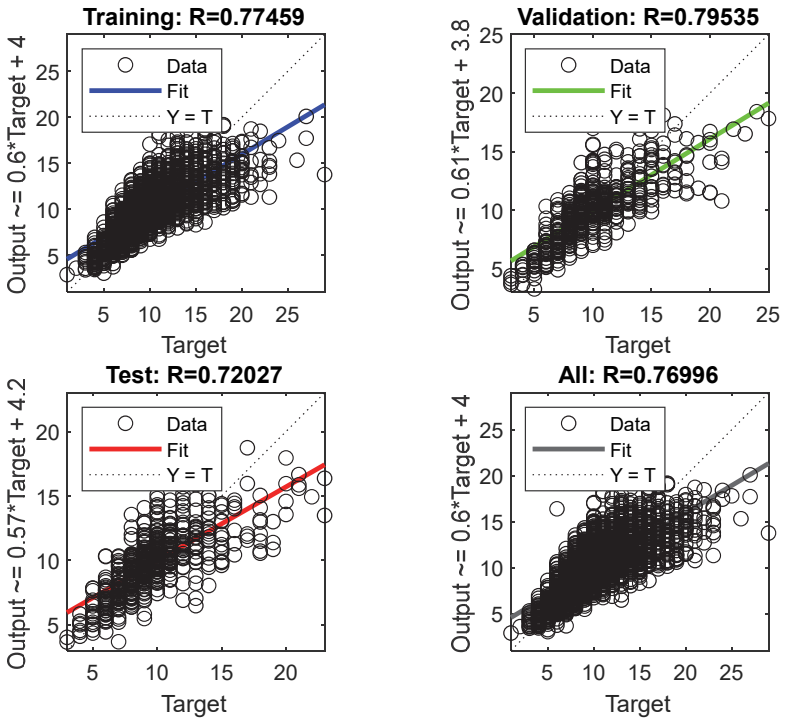

Figure 14: Regression analysis in Y direction of displacement prediction for model 2 at node 8.

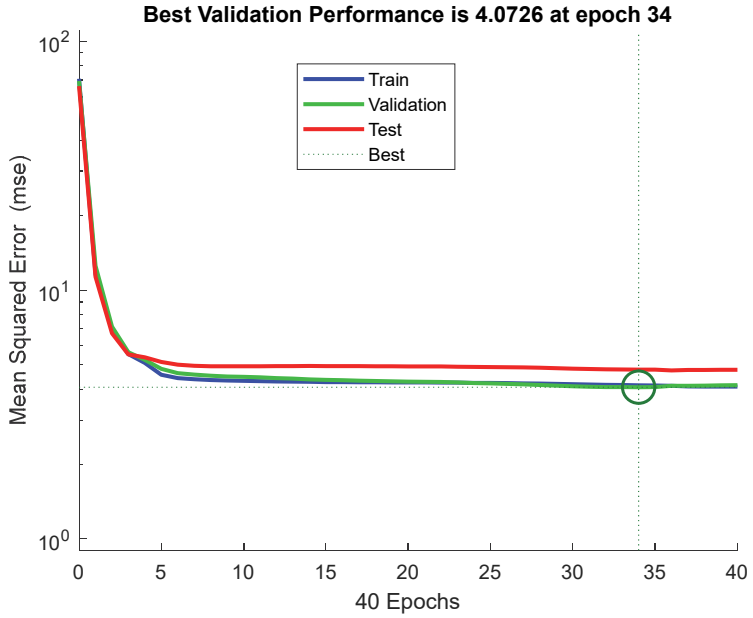

Figure 15: Prediction of displacement in Y direction for model 2 at node 8.

No	Important Vertical Peak Acceleration (g)	Vertical Peak Stress (MPa)	Vertical Peak Strain	Initial crack length (mm)	Vertical Displacement (mm)
1	-0.06228	0.00364	3.87191E-4	2778	0.49187
2	0.06384	-0.00374	-4.15158E-4	2778	0.81999
3	-0.08703	-0.00484	-5.59286E-4	2778	-0.20928
4	0.08813	0.00498	5.89115E-4	2778	0.96371
5	-0.0911	-0.00513	-5.89344E-4	2778	-0.67519
6	0.09609	0.00539	6.65428E-4	2778	0.60006
7	0.08894	-0.00395	5.04661E-4	2778	-1.59723
8	-0.08411	0.00451	-4.57753E-4	2778	-1.32669
9	0.07111	0.00402	5.3166E-4	2778	1.05664
10	-0.07159	-0.00393	-4.78772E-4	2778	-0.68074
11	-0.07212	-0.00371	-4.42859E-4	2778	1.52171
12	0.06941	0.00386	5.06271E-4	2778	1.18099
13	0.06717	-0.00381	-5.26548E-4	2778	-0.56321
14	-0.06425	0.00397	5.02833E-4	2778	0.69203
15	0.06058	-0.00362	4.38587E-4	2778	-1.17325
16	-0.06356	0.0034	-4.2151E-4	2778	-1.63809
17	0.06251	-0.00364	-4.58134E-4	2778	-1.32084
18	-0.06359	0.00334	4.37875E-4	2778	0.62052
19	-0.06205	-0.00407	-5.43534E-4	2778	-0.45421
20	0.06243	0.00304	-4.31483E-4	2778	1.38419
21	-0.0695	0.00335	4.65704E-4	2778	1.3113
22	0.066	-0.00347	4.06485E-4	2778	-0.39103
23	-0.06804	0.00304	-4.43368E-4	2778	0.78891
24	0.06476	-0.00411	-4.31212E-4	2778	-0.95975
25	0.07177	-0.00363	4.97951E-4	2778	0.32627
26	-0.0713	0.00394	-4.34561E-4	2778	-1.36753
27	-0.07217	-0.00427	4.53222E-4	2778	-1.07084
28	0.0667	0.00341	-4.10302E-4	2778	0.90474
29	-0.06252	0.00442	-4.36056E-4	2778	2.11807
30	0.06705	-0.00368	4.91303E-4	2778	1.01959
31	0.06841	0.00309	-4.46954E-4	2778	-0.72574
32	-0.07263	-0.00333	4.76944E-4	2778	-1.69437

Table 9: Data used in ANNs for model 2 at node 12.

-	Training	Validation	Test	Number of layers in ANNs
R^2	0.78406	0.78312	0.71877	3
MSE	3.9838	4.4124	4.7717	3

Table 10: R^2 and MSE results ANNs for model 2 at node 12.

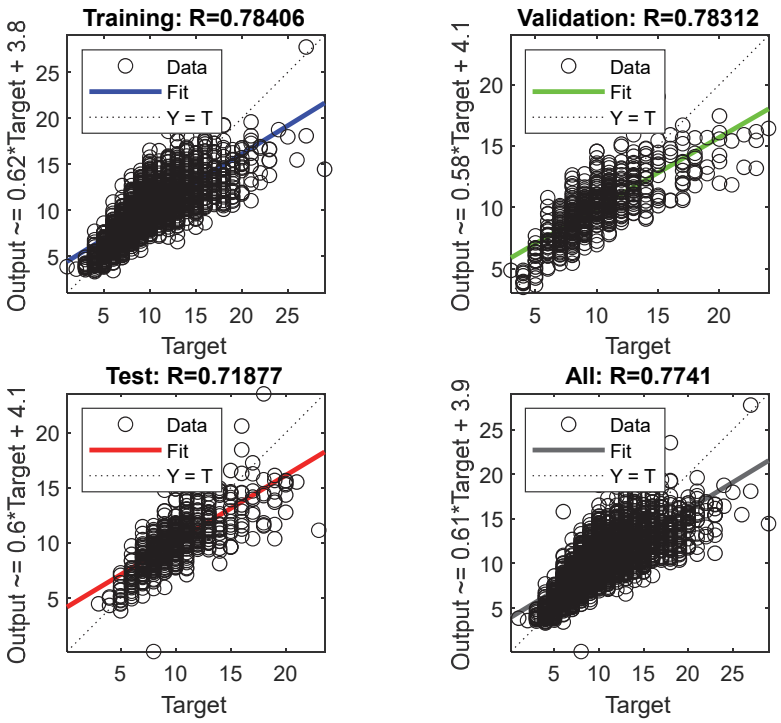

Figure 16: Regression analysis in the Y direction of displacement prediction for model 2 at node 12.

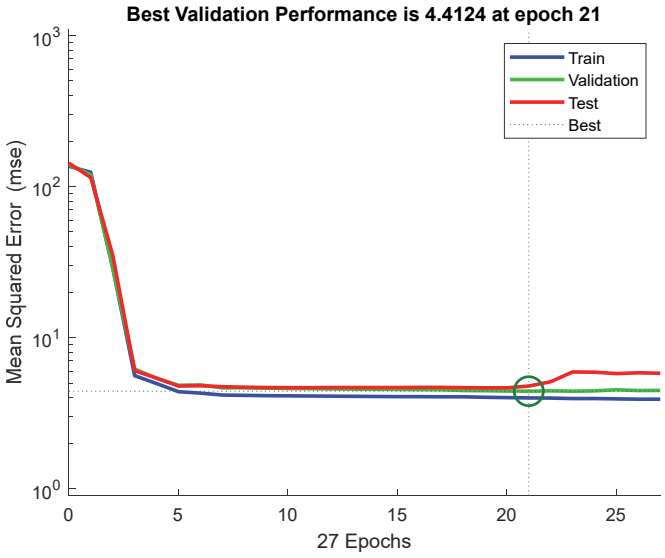

Figure 17: Prediction of displacement in Y direction for model 2 at node 12.

THE CRACK MORPHOLOGY OF LANDFILL

The MSW in each region possesses different mechanical properties. The present simulation work has been done numerically for designing the landfill clay cover. Figs. 18 and 19 illustrate the tension crack in the landfill clayey cover. In Fig. 18, a single initial tension crack in the clayey cover of the landfill is created. This crack we have simulated in the present work, while in Fig. 19, the initial multidirectional tension crack in the clayey cover of the landfill has been developed. Considering the clayey landfill cover for controlling leachate, as presented in the literature [24-25], the seismic stability design of the landfill plays an important role by considering the thickness of the clayey landfill cover when constructing the landfill.

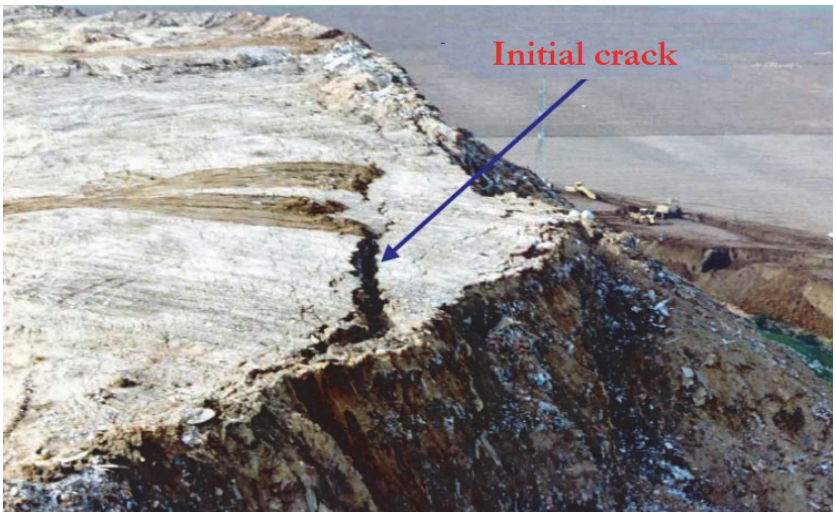

Figure 18: The single initial tension crack in the landfill [4].

In each region, MSW has different mechanical properties depending on how it is produced, how it is compacted during landfill construction, how temperature affects the mechanical properties of MSW, and how much moisture it contains due to climate and leachate drainage, etc. Predictions of landfill seismic stability are supported by simulations of landfill design. Landfill sliding and shear failures can be predicted based on landfill design. Fig. 19 shows how the initial tension crack of the landfill can interact during the seismic loading on the landfill. The crack interaction causes landfill failure acceleration.

Figure 19: The initial multidirectional tension crack in the cracked zone of the landfill [5].

CONCLUSION

A simulation was conducted to simulate the displacement of the landfill covered by cracked clay under seismic loading. Rankine's theory, the Phantom Node Method, and the Levenberg-Marquardt Algorithm were used to simulate, predict, and validate the numerical simulation results. Stress, strain, and length of the crack were selected to predict displacement at critical points. ANNs were used to predict displacement in the Y direction for the selected nodes. The following findings were achieved in the present study:

- In each model, the crack initiation, crack shape modification, deformation speed, and shape are distinct. These phenomena are associated with clay landfill cover. The crack propagation in the landfill model is related to the damage magnitude.
- In response to nonlinear seismic acceleration, crack morphology changes and impacts seismic acceleration transmission and landfill seismic stability. The nature of seismic acceleration (g) in both studied models determines the failure mechanism. Furthermore, the landfill clay cover thickness influences crack propagation.
- Models 1 and 2 show different patterns of seismic acceleration transfer and dissipation. Based on the nonlinearity in shear stress-strain for models 1 and 2, it can be concluded that landfill deformation is associated with landfill model design.
- The nature of the seismic acceleration is an important factor in the collapse of the landfill model.
- The clay with a thickness of 0.6–1.5 m controls the leachate, but it is not good enough to ensure landfill stability during earthquakes. A suitable thickness of clay needs to be chosen based on seismic stability analysis.

REFERENCES

[1] Moradian, F., Ramavandi, B., Jaafarzadeh, N. Kouhgardi, E. (2020). Effective treatment of high-salinity landfill leachate using ultraviolet/ultrasonication/peroxymonosulfate system. Waste Manage. 118, pp. 591-599. DOI: 10.1016/j.wasman.2020.09.018.

[2] Baderna, D., Caloni, F., Benfenati, E. (2019). Investigating landfill leachate toxicity in vitro: A review of cell models and endpoints. Environ. Int., 122, pp. 21-30. DOI: 10.1016/j.envint.2018.11.02.

[3] Visvanathan, C., Pokhrel, D., Cheimchaisri, W., Hettiaratchi, J.P.A., Wu, J.S. (1999). Methanotrophic activities in tropical landfill cover soils: effects of temperature, moisture content and methane concentration. Waste Manag. Res. 17, pp. 313-323. DOI: 10.1034/j.1399-3070.1999.00052.x

[4] Huvaj-Sarihan, N., Stark, T. D. (2008). Back-Analyses of Landfill Slope Failures. 6th Conference of the International Conference on Case Histories in Geotechnical Engineering. Arlington, VA.

[5] Kocasoy, G., K, Curi. (1995). The Umraniye-Hekimbasi Open Dump Accident. Waste Manag. Res. 13 (4), pp. 305-314.

[6] Psarropoulos, P.N., Tsompanakis, Y., Karabatsos, Y. (2007). Effects of local site conditions on the seismic response of municipal solid waste landfills. Soil Dyn. Earthq. 27, pp. 553–563. DOI:10.1016/j.soildyn.2006.10.004

[7] Matasovic, N., Kavazanjian, E.J., Augello, AJ., Bray, J.D., Seed, R.B.(1995). Solid waste landfill damage caused by 17 January 1994 Northridge earthquake. In: Woods MC, Seiple RW, editors. The Northridge California earthquake in 17 January 1994, vol. 116. Sacramento, California, USA: California Department of Conservation, Division of Mines and Geology Special Publication.

[8] Newmark, N.M. (1965). Effect of earthquakes on dams and embankments. Geotechnique. 15(2), pp. 139-60.

[9] Namdar, A., Dong, Y. (2020). The embankment-subsoil displacement mechanism, Mater. Des. Process Comm. e155, pp. 1-4. DOI: 10.1002/mdp2.155.

[10] Namdar, A. 2021. Design geometry of the embankment for minimize nonlinear displacement. Mater. Des. Process Comm. e209. DOI: 10.1002/mdp2.209.

[11] Namdar, A., Satyam, N. (2021). Characterization displacement of multilayered soils using smoothing seismic data, numerical analysis and probabilistically statistics analysis. SN Applied Sciences. 3(621). DOI:10.1007/s42452-021-04611-7.

[12] Guo, L. Li, W. Namdar, A. (2021). Using recycled aggregate for seismically monitoring of embankment-subsoil model. Case Stud. Constr. Mater. 15 (3) e00605. DOI:10.1016/j.cscm.2021.e00605.

[13] Saygili, G., Rathje, E.M. (2008). Empirical predictive models for earthquake-induced sliding displacements of slopes. J. Geotech. Geoenviron. Eng. 134 (6), pp. 790–803.

[14] Rathje, E.M., Saygili, G. (2009). Probabilistic assessment of earthquake-induced sliding displacements of natural slopes. Bull. N. Z. Soc. Earthq. 42 (1), pp. 18-27.

[15] Hsieh, S.Y., Lee, L.T. (2011). Empirical estimation of the Newmark displacement from the Arias intensity and critical acceleration. Eng. Geol. 122 (1-2), pp. 34–42.
[16] Ramakrishna Annapareddy, V.S., Pain, A., Sufian, A., Godas, S., Scheuermann, A. (2023). Influence of heterogeneity and elevated temperatures on the seismic translational stability of engineered landfills. Waste Manage. 158, pp. 1-12. DOI: 10.1016/j.wasman.2023.01.004.
[17] Kavazanjian Jr, E., Gutierrez, A. (2017). Large scale centrifuge test of a geomembrane-lined landfill subject to waste settlement and seismic loading. Waste Manage. 68, pp. 252-262. DOI:10.1016/j.wasman.2017.01.029
[18] Zania, V., Tsompanakis, Y., Psarropoulos, P.N. (2010). Seismic displacements of landfills and deformation of geosynthetics due to base sliding. Geotext. Geomembr. 28, pp. 491-502. DOI: 10.1016/j.geotexmem.2009.12.013.
[19] Yazdani, R., Campbell, J.L., Koerner, G.R. (1995). Long-term in situ strain measurements of a high density polyethylene geomembrane in a municipal solid waste landfill. In: Geosynthetics '95 Conference Proceedings, pp. 893–906.
[20] Cortellazzo, G., Russo, L.E., Busana, S., Carbone, L., Favaretti, M., Hangen, H. (2022). Field trial of a reinforced landfill cover system: performance and failure. Geotext. Geomembr. 50, pp. 655-667. DOI: 10.1016/j.geotexmem.2022.03.007.
[21] Hamdi, N., Srasra, E. (2013). Hydraulic conductivity study of compacted clay soils used as landfill liners for an acidic waste. Waste Manage. 33, pp. 60-66. DOI: 10.1016/j.wasman.2012.08.012.
[22] Aswathy. C.M., Sunil, B.M. (2022). Effect of ammonia on the hydraulic conductivity and adsorption characteristics of lithomargic clay - bentonite barrier in landfills. J. Environ. Chem. Eng. 10, 108750. DOI: 10.1016/j.jece.2022.108750.
[23] Emmanuel, E., Anggraini, V., Raghunandan, M.E., Asadi, A. (2020). Utilization of marine clay as a bottom liner material in engineered landfills, J. Environ. Chem. Eng. 8, 104048, DOI: 10.1016/j.jece.2020.104048.
[24] Daniel, D.E. (1993). Geotechnical Practice for Waste Disposal, Chapman & Hall Ltd, London, 1993, pp. 137–163.
[25] Rowe, R.K., Quigley, R.M., Booker, J.R. (1995). Clayey Barrier Systems for Waste Disposal Facilities, E & FN Spon, London, p. 390.
[26] Namdar, A. (2020). Forecasting bearing capacity of the mixed soil using artificial neural networking. Frat. ed Integrita Strutt. 14 (53), pp. 285-294. DOI:10.3221/IGF-ESIS.23.22
[27] Omar, M., Shanableh, A., Mughieda, O., Arab, M., Zeiada, W., Al-Ruzouq, R. (2018). Advanced mathematical models and their comparison to predict compaction properties of fine-grained soils from various physical properties. Soils Found. 58, pp. 1383-1399. DOI:10.1016/j.sandf.2018.08.004
[28] Bordonaro, G.G., Leardi, R., Diviani, L., Berto, F. (2018). Design of Experiment as a powerful tool when applying Finite Element Method: a case study on prediction of hot rolling process parameters. Frat. ed Integrita Strutt. 12(44), pp. 1-15. DOI: 10.3221/IGF-ESIS.44.01.
[29] Foti, P., Berto, F., Filippi, S. (2018). Fatigue assessment of welded joints by means of the Strain Energy Density method: Numerical predictions and comparison with Eurocode 3: Numerical predictions and comparison with Eurocode 3. Frat. ed Integrita Strutt. 13(47), pp. 104-125. DOI: 10.3221/IGF-ESIS.47.09.
[30] Rankine, W. (1857). On the stability of loose earth. Philosophical Transactions of the Royal Society of London, 147.
[31] Budhu, M. (2010). Soil mechanics and foundations. John Wiley & Sons, Inc.
[32] Craig, R.F. (2004). Soil Mechanics. Spon Press. Taylor & Francis Group.
[33] Namdar, A. (2021). The boundary condition simulation quality for embankment seismic response. Eng. Fail. Anal. 126, 1054a91. DOI: 10.1016/j.engfailanal.2021.105491
[34] Center for Engineering Strong Motion Data (CESMD), https://strongmotioncenter.org/
[35] Singh, M.K., Sharma, J.S., Fleming, I.R., (2009). A design chart for estimation of horizontal displacement in municipal landfills. Waste Manage. 29, pp. 1577-1587. DOI: 10.1016/j.wasman.2008.10.003.
[36] Matasović, N., Kavazanjian Jr, E., (1998). Cyclic characteristics of OII landfill soil waste. J GEOTECH GEOENVIRON. 124(3), pp. 197-210. DOI: 10.1061/(ASCE)1090-0241(1998)124:3(197).
[37] Seo, B. (2008). Compositional effects on the mechanical properties of municipal solid waste. Arizona State University. Doctoral thesis. UMI Number: 3339537.
[38] Davis, E.H., Christian, J.T. (1971). Bearing capacity of anisotropic cohesive soil. J. Soil Mech. Found. Divis. ASCE 97 (5), pp. 753-769.
[39] Jamshidi Chenari, R., Bathurst, R.J. (2023). Influence of geosynthetic stiffness on bearing capacity of strip footings seated on thin reinforced granular layers over undrained soft clay. Geotext. Geomembr. 51, pp. 43-55. DOI: 10.1016/j.geotexmem.2022.09.006.
[40] Babuska, I., Melenk, J.M. (1998). The partition of unity method. Int J Numer Methods Eng. 40(4), pp. 727-758. DOI: 10.1002/(SICI)1097-0207(19970228)40:4<727::AID-NME86>3.0.CO;2-N
[41] Namdar, A., Karimpour-Fard, M., Muhammad, N. (2022). The seismic resistance simulation for cracked clayey backfill. Eng. Fail. Anal. 140, 106616. DOI: 10.1016/j.engfailanal.2022.106616.
[42] Namdar, A., Berto, F., Muhammad, N. (2022). The displacement simulation for cracked earth structure with different geometry. Procedia Struct. 41, pp. 394-402. DOI: 10.1016/j.prostr.2022.05.045.

[43] Belytschko, T., Black. T. (1999). Elastic crack growth in finite elements with minimal remeshing. Internat. J. Numer. Methods Engrg. 45, pp. 601-620. DOI: 10.1002/(SICI)1097-0207(19990620)45:5<601::AID-NME598>3.0.CO;2-S
[44] Moes, N., Dolbow, J., Belytschko, T. (1999). A finite element method for crack growth without remeshing. Internat. J. Numer. Methods Engrg. 46, pp. 131-150.
[45] Hansbo, A., Hansbo, P. (2004). A finite element method for the simulation of strong and weak discontinuities in solid mechanics. Comput Methods Appl Mech Eng. 193(33), pp. 3523-3540. DOI: 10.1016/j.cma.2003.12.041.
[46] Rabczuk, T., Zi, G., Gerstenberger, A. (2008). Wall WA. A new crack tip element for the phantom-node method with arbitrary cohesive cracks. Int J Numer Methods Eng. 75(5), pp. 577-599. DOI: 10.1002/nme.2273.
[47] Mororó, L.A.T., Poot, A., Meer, F.P. van der. (2022). Skeleton curve and phantom node method for the Thick Level Set approach to fracture. Eng. Fract. Mech. 268, pp. 108443. DOI: 10.4121/1940084 9.v1.
[48] van der Meer, F.P., Sluys, L.J. (2009). A phantom node formulation with mixed mode cohesive law for splitting in laminates. Int J Fract. 158, pp. 107–124. DOI: 10.1007/s10704-009-9344-5.
[49] Cha, D., Zhang, H., Blumenstein, M. (2011). Prediction of maximum wave-induced liquefaction in porous seabed using multi-artificial neural network model. Ocean Eng. 38(7), pp. 878–887. DOI: 10.1016/j.oceaneng.2010.08.002.
[50] Levenberg, K. (1944). A Method for the Solution of Certain Non-Linear Problems in Least Squares. Q Appl Math. 11(2), pp. 164-168.
[51] Ken, B., Joan, D. (2007). Calculus Concepts and Methods. Cambridge University Press. p. 190. OCLC 717598615.
[52] Math works guidance. https://nl.mathworks.com/help/deeplearning/ref/trainlm.html
[53] Devore, J., Farnum, N., Doi, J. (2014). Applied Statistics for Engineers and Scientists. Publisher Richard Stratton.

NOMENCLATURE

E	Modulus elasticity
E_u	Undrained modulus elasticity
ϕ	Friction angle
ϕ_u	Undrained friction angle
ψ	Dilatancy angle
C	Cohesion
C_U	Undrained shear strength
γ	Unit weight
γ_c	Undrained unit weight
ν	Poisson's ratio
ν_c	Undrained poisson's ratio
G	Shear modulus
Z_0	Cracked zone
S_z	Solid zone
Kp	Passive earth pressure coefficients
Ka	Active earth pressure coefficients
θ_a	Rankine active state of slip planes
θ_p	Rankine passive state of slip planes
P_p	Lateral earth force in passive state
P_a	Lateral earth force in active state
$\left(\sigma_x^{'}\right)_a$	Lateral earth pressure in passive state
$\left(\sigma_x^{'}\right)_p$	Lateral earth pressure in active state
$\sigma_z^{'}$	Effective stresses
γ'	Effective density
γ_{sat}	Saturated density
γ_w	Water density
$N_i(x)$	Standard finite element shape functions
u_i	Standard finite element unknowns
$N_i^*(x)$	Partition of unity

$\tilde{N}\mp(x)$ Global enrichment function

a_i Unknowns associated with the enrichments

Γ_s Crack path

Ω_A Shaded area is portion of a new element A

Ω_B Shaded area is portion of a new element B

N Standard finite element method shape functions

U_A Displacement in node A

U_B Displacement in node B

d Obtained nonlinear displacement

d_p Predicted displacement by ANNs

$\overline{D}_o$ Mean value of obtained nonlinear displacement.

J Jacobian matrix

H Hessian matrix

e Vector of network errors

g_k Gradient

W_{k+1} Updated weights in the Levenberg-Marquardt algorithm